PERGAMON

International Journal of Heat and Mass Transfer 41 (1998) 2743–2756

International Journal of HEAT and MASS TRANSFER

On the evolution of double-diffusive intrusions into a stably stratified liquid: a study of the layer merging process

E. Jurjen Kranenborg, Henk A. Dijkstra*

Institute for Marine and Atmospheric Research, Utrecht University, Utrecht, The Netherlands

Received 6 March 1997; and in final form 25 November 1997

Abstract

The nonlinear evolution of double-diffusive instabilities into a laterally heated stably stratified motionless liquid is studied through direct numerical simulation in a two-dimensional set-up. In this paper, we consider liquids which are initially stratified through a constant salt gradient. The stages of evolution of the intrusions and their spatial scales correspond well with those observed in laboratory experiments. A central process in the evolution is that of layer merging. A particular case of layer merging is analysed in detail and a new physical description of this process is proposed, to which we refer as 'layer sandwiching'.

Nomenclature

A aspect ratio
E_k dimensionless kinetic energy
E_p dimensionless potential energy
Fo Fourier number
g gravitational acceleration [m s^{-2}]
H height of the container [m]
$\mathcal{H}_d$ dimensionless diffusive lateral heat transport
K dimensionless lateral temperature gradient
L length of container [m]
Le Lewis number
Nu Nusselt number
$\overline{Nu}$ vertically integrated Nusselt number
Pr Prandtl number
R buoyancy ratio
Ra_η thermal Rayleigh number based on η
Ra_ζ thermal Rayleigh number based on ζ
Ra_T thermal Rayleigh number
Ri Richardson number
S dimensionless salinity
Sh Sherwood number
$\overline{Sh}$ horizontally integrated Sherwood number
t dimensionless time
t_0 dimensionless heat-up time
T dimensionless temperature
u dimensionless horizontal velocity
U^* characteristic horizontal velocity [m s^2]
w dimensionless vertical velocity
x dimensionless horizontal coordinate
z dimensionless vertical coordinate.

Greek symbols

α thermal expansion coefficient [K^{-1}]
β solutal expansion coefficient [—]
ΔS vertical salinity difference [—]
ΔT horizontal temperature difference [K]
ζ internal vertical lengthscale [m]
η internal vertical lengthscale [m]
κ_S solutal diffusivity [m^2 s^{-1}]
κ_T thermal diffusivity [m^2 s^{-1}]
ν kinematic viscosity [m^2 s^{-1}]
ρ density [kg m^{-3}]
ϕ_0 initial salinity gradient [m^{-1}]
ψ dimensionless streamfunction
ω dimensionless vorticity.

Subscripts

cr critical
i initial
f final
0 reference value.

Superscript

* indicating dimension.

*Corresponding author. Tel.: 31-30-2533276; fax: 31-30-2543163; e-mail: h.a.dijkstra@fys.ruu.nl.

0017-9310/98 $19.00
PII: S0017-9310(98)00008-8

1. Introduction

The discovery of fine structure within the ocean has stimulated detailed studies of small-scale mixing processes. One of these processes is that of double-diffusive convection, i.e. convection in a stably stratified liquid due to different diffusivities of two components [1]. Associated with this small scale mixing process is the appearance of well mixed layers, separated by very stable interfaces over which only diffusive transport is possible. The vertical temperature and salinity structure associated with these layers show characteristic step structures. Such step structures in temperature and salinity have been found over large areas in the upper ocean. Since the presence of layers significantly influences the transport of heat and salt, double-diffusive convection is a potentially important transport mechanism e.g. for heat and salt in the ocean. Apart from the oceanographic context, there are many technological motivations to study these type of flows, for example crystal growth and the heat storage in solar ponds [2].

A typical example of layer formation is that of a liquid which is stably stratified through a constant salt gradient ϕ_0 and which is heated through a lateral temperature gradient. The buoyancy driven flow becomes unstable when a critical value of the lateral temperature difference is exceeded. The instabilities are shear driven for small ϕ_0, but when ϕ_0 is large the flow becomes unstable to double-diffusive instabilities [3]. When a parcel of liquid near the heated wall moves upward, it retains almost all of its salt due to the very small salt diffusivity but loses its heat relatively fast. The parcel rises to a level where its density is equal to that of the surrounding liquid and because of continuity it is then forced to move laterally; a layered flow pattern eventually results.

Much information on the layer formation process was obtained from laboratory experiments. These were performed either in narrow slots or in wide tanks, using different temperature rise curves at the heated wall and with different initial conditions. With respect to the latter, two different types can be distinguished. In singly stratified experiments, only a salinity gradient is initially present, whereas the temperature is homogeneous. In doubly stratified experiments, a destabilizing temperature gradient is also initially present such that the layer is still stably stratified. In early singly stratified experiments in narrow slots [4], it was found that when a critical value of a Rayleigh number Ra_η based on the length scale

$$\eta = \frac{\alpha \Delta T}{\beta \phi_0} \tag{1}$$

is exceeded, layers appear over the whole length of the heated wall. Here ΔT is the imposed lateral temperature difference and α, β the thermal and solutal coefficients in the (linear) equation of state, respectively. The length scale η is directly related to the movement of a heated liquid parcel to its neutrally buoyant level. The critical value of Ra_η was determined from experiments and given approximately by $Ra_{\eta,\mathrm{cr}} = 1.5 \times 10^4$. In the supercritical flow regime, also called simultaneously formed layer regime, eventually layers with a characteristic thickness η develop [4–6]. Below the critical value $Ra_{\eta,\mathrm{cr}}$ the layers grow successively from the horizontal walls and layers with a larger scale than η develop.

A detailed experimental study of the evolution of intrusions in a constant vertical salt gradient was presented by ref. [7]. One of the sidewalls of a wide container (aspect ratio about 2.4) was heated using a prescribed temperature-rise curve. After a characteristic time t_0, a nearly constant lateral temperature difference ΔT was obtained. The flows for both the heat/salt and the heat-/sugar system for different time constants t_0 in the range 75–8000 [s] were monitored. Three different stages of development of the intrusions were distinguished. The thermal boundary layer which develops at the heated wall becomes unstable and initial layers appear. It was shown that the stability characteristics in a wide container are essentially the same as in a narrow slot [3] and do not depend on the details of the heating curve. Besides η, ref. [7] also used a (ΔT-independent) length scale $\zeta = (\nu \kappa_S / g \phi_0)^{1/4}$ to represent their results, indicating that the initial layer thickness depends only on the salinity gradient, the acceleration due to gravity g, the kinematic viscosity ν and the diffusivity of salt κ_S. In this formulation, an initial layer scale $h_i = 29.1\,\zeta$ was found and the critical Rayleigh number $Ra_{\zeta,\mathrm{cr}}$ based on ζ was about 50.

A second stage of evolution is the transition of layers with initial thickness h_i to a slightly larger thickness due to initial layer merging. Reference [7] gives arguments that this initial merging is due to a subsequent instability of the flow. Since Ra_ζ depends on ΔT, this value changes during the evolution of the flow. If the final value of Ra_ζ in a particular experiment is larger than 75, layer merging occurs at a value $Ra_\zeta = 75$. If the final value is smaller than 75, layer merging eventually occurs but it is observed after a much longer time. This is consistent with the results in ref. [5], where t_0 is small and immediately layers with a final thickness are observed. Here, the initial layers have a very short lifetime and the merging stage is too short to be observed.

In the third stage of evolution, the layers approach their final thickness h_f which is characterized by the length scale η; ref. [7] finds the relation $h_f = 0.62\,\eta$ and a similar relation is obtained by ref. [5]. In the approach to this final layer thickness, subsequent merging of layers occurs. It appears that this evolution is rather complicated, since nearly identical experiments show a different evolution and merging sequence. No specific criteria for subsequent merging could be found and it was suggested that the behavior of the flow is chaotic after the instability of the initial layers [7].

More detail to the description of the subsequent layer

merging process was added through the singly stratified experiments of ref. [8]. Their results are consistent with those of ref. [7] in that the initial merging occurs uniformly along the entire vertical sidewall. A subsequent merging process was monitored through vertical temperature profiles near the heated wall. As they describe: "...the merging process commenced with one layer propagating slightly faster than its neighbour immediately below, and subsequently merging together...". They also find that merging is initiated at the heated wall and is completed at the extremity of the intrusion. It is suggested that the thermal boundary layer near the heated wall penetrates the salinity interface and locally destroys the salinity step.

Despite these descriptions from laboratory experiments, the physics of the layer merging process is still unclear. Theoretical work has mainly focussed on the initial stage of layer formation as an instability of a weak buoyancy driven background flow [3] and its weakly nonlinear evolution [9]. Further progress was made through numerical simulation of the intrusions, which has only been done in two-dimensional configurations. Within narrow slots, ref. [10] studied the evolution of the flow in both supercritical and subcritical flow regimes and found that in both regimes layers grow from the horizontal walls. Only in the supercritical case the layered structure finally extends over the entire slot, in agreement with their experimental results. In ref. [11], flows in a narrow slot configuration are studied numerically, where a salt difference ΔS was maintained between top and bottom, similar to their experimental set-up [6]. This configuration is interesting because it allows for steady states to occur. In additional to the simultaneously and successively formed layer regimes, they find two other regimes of flow, a unicellular regime and a stagnant flow regime.

The latter configuration motivated the bifurcation studies of refs. [12–14] for narrow slot configurations. Main result of these studies is that many steady flow patterns are possible, but that most of these flows are unstable. Within the unicellular flow regime, the structure of stable steady states was shown to be simple and to consist of only a strong thermally driven cell. However, the unstable steady states (multicellular flows) were shown to be physically relevant. The flow can remain quite long near one of these states and a long preconditioning process is needed to initiate the instability. The boundary between the unicellular flow regime and the successively formed layer regime could be associated with an instability of the unicellular flow. However, no clear boundaries were identified between the other regimes.

In this paper, we continue the investigation of the evolution of intrusions in the supercritical case. We study the evolution of intrusions into a constant salinity gradient through a high resolution direct numerical simulation in a two-dimensional set-up. Although the flows in laboratory experiments are obviously three-dimensional, it is shown that the same stages of development and corresponding spatial and temporal scales are found. Hence, the essential physics of the evolution of the intrusions is captured by a two-dimensional model. Main contribution of this paper is a detailed analysis of a typical case of layer merging. We propose a new description of the physics of the layer merging process, to which we refer to as 'layer sandwiching', which involves a feedback between differential entrainment and changes in the layer thickness of neighboring layers.

2. Formulation

A two-dimensional rectangular container (length L and height H) is filled with a Newtonian liquid with a kinematic viscosity ν and stratified through heat and salt with constant thermal diffusivity κ_T and solutal diffusivity κ_S. The density ρ of the liquid depends linearly on temperature and salinity and is given by $\rho(T^*, S^*) = \rho_0(1-\alpha(T^*-T_0)+\beta(S^*-S_0))$, where T_0 and S_0 are (constant) reference values of the temperature and the salinity. Let ΔS and ΔT be a characteristic vertical salinity and horizontal temperature difference. The governing equations are non-dimensionalized using scales H, H^2/κ_T and κ_T/H for length, time and velocity, respectively. A dimensionless temperature and salinity are defined by $T=(T^*-T_0)/\Delta T$ and $S=(S^*-S_0)/\Delta S$. In terms of the streamfunction ψ and vorticity ω, where

$$u=\frac{\partial\psi}{\partial z}, \quad w=-\frac{\partial\psi}{\partial x}, \quad \omega=-\nabla^2\psi \tag{2a}$$

the full equations, with the usual Boussinesq approximation, are given by

$$Pr^{-1}\left(\frac{\partial\omega}{\partial t}+\frac{\partial\psi}{\partial z}\frac{\partial\omega}{\partial x}-\frac{\partial\psi}{\partial x}\frac{\partial\omega}{\partial z}\right)=\nabla^2\omega+Ra_T\left(\frac{\partial T}{\partial x}-R\frac{\partial S}{\partial x}\right) \tag{2b}$$

$$\frac{\partial T}{\partial t}+\frac{\partial\psi}{\partial z}\frac{\partial T}{\partial x}-\frac{\partial\psi}{\partial x}\frac{\partial T}{\partial z}=\nabla^2 T \tag{2c}$$

$$\frac{\partial S}{\partial t}+\frac{\partial\psi}{\partial z}\frac{\partial S}{\partial x}-\frac{\partial\psi}{\partial x}\frac{\partial S}{\partial z}=Le^{-1}\nabla^2 S. \tag{2d}$$

The dimensionless parameters which appear in the equations above are defined as

$$Ra_T=\frac{g\alpha\Delta T H^3}{\nu\kappa_T}, \quad R=\frac{\beta\Delta S}{\alpha\Delta T},$$

$$Pr=\frac{\nu}{\kappa_T}, \quad Le=\frac{\kappa_T}{\kappa_S}, \quad A=\frac{L}{H}. \tag{3}$$

The relative importance of saline vs. thermal buoyant forcing is given by the buoyancy ratio R. The lengthscale

η and the Rayleigh number Ra_η can be expressed into the parameters in (3) as

$$\eta = H/R; \quad Ra_\eta = Ra_T/R^3. \tag{4}$$

In this paper we investigate the development of intrusions into a constant salinity gradient only for a square container ($A = 1$). Initial conditions correspond to a motionless solution for which the salinity varies linearly with height, i.e.

$$t = 0: \quad \psi(x,z) = \omega(x,z) = T(x,z) = 0; \quad S(x,z) = 1 - z. \tag{5a}$$

At the left sidewall, a heating rise curve is prescribed as

$$T(x = 0, z, t) = 1 - \exp\left(-\frac{t}{t_0}\right) \tag{5b}$$

similar to that used in the experiments of ref. [7]. The right sidewall is kept at the initial temperature of the bulk. The applied lateral temperature gradient is therefore constant, apart from a short initial transient phase. The upper and lower walls are isothermal. A stable salinity gradient is maintained by prescribing a constant salinity difference between the upper and lower walls; the lateral walls are impermeable to salt. In dimensionless form the remaining boundary conditions are

$$x = 0: \quad \frac{\partial S}{\partial x} = 0; \quad x = 1: \quad T = 0, \quad \frac{\partial S}{\partial x} = 0;$$
$$z = 0: \quad S = 1, \quad \frac{\partial T}{\partial z} = 0; \quad z = 1: \quad S = 0, \quad \frac{\partial T}{\partial z} = 0. \tag{5c}$$

At all boundaries no-slip conditions for velocity are prescribed.

3. Results

A 'reference' numerical simulation is defined by the values of the parameters as given in Table 1. It appears difficult to perform accurate simulations in the range of buoyancy ratios used in laboratory experiments. Both in ref. [7] and in ref. [8], the buoyancy ratio R is within the range 30–50. This is desired in experiments, because many layers develop and their average thickness can be well determined. Numerically, one does not want to simulate that many layers, because of the very high resolution required. In the 'reference' simulation, the buoyancy ratio is therefore chosen smaller than in experiments, in order to generate a smaller number of layers. At constant η, this means that the container height H is decreased with respect to that in experiments. Consequently, the horizontal walls of the container may have more influence on the flow development than in experiments.

The governing equations and boundary conditions are discretized spatially using second order accurate central differences on an equidistant grid. Because of the rapid evolution of the flow an explicit (first order accurate) Euler method is used to integrate in time. High spatial resolution is necessary to resolve the details of the flow, especially to resolve the large gradients in the salt field. The thickness of these saline boundary layers scales with $Pe^{-(1/2)}$, where $Pe = (U^* H/\kappa_S)$ and U^* is a characteristic horizontal velocity scale of the convection within the layers. For the reference case, with $U^* = 5 \times 10^{-5}$ [m s^{-1}], $Pe = 10^4$ and the estimated interface thickness is about 0.01 H. To have at least two points within each interface, an equidistant grid of 201 * 201 points is used for this simulation. The dimensionless timestep used for the calculations is of order $O(10^{-8})$, total CPU time is of order $O(10^5)$ [s] on a Cray C90.

Table 1
Values of both dimensionless and dimensional model parameters

Dimensionless quantities	
A	1
Le	100
Pr	7
R	5
Ra_η	$5 \cdot 10^4$
Ra_S	$3.125 \cdot 10^7$
Ra_T	$6.25 \cdot 10^6$
t_0	$1 \cdot 10^{-3}$
Dimensional quantities	
H	0.2 (m)
L	0.2 (m)
κ_S	$1 \cdot 10^{-9}$ (m^2 s^{-1})
κ_T	$1 \cdot 10^{-7}$ (m^2 s^{-1})
ν	$7 \cdot 10^{-7}$ (m^2 s^{-1})

From the results in ref. [14], it can be deduced that the parameters of the reference simulation are such that eventually a unicellular flow is reached at $t \to \infty$. In this paper, we focus on the initial stages of evolution towards this flow. Several flow characteristics are presented in Section 3.1 and a particular case of layer merging is observed. Thereafter, we focus on the signatures of layer merging in the heat and mass transfer rates (Section 3.2), the overall energy balances (Section 3.3) and on particular flow details (Section 3.4).

3.1. Flow characteristics

In all simulations below, the dimensionless time t_0 in (5b) was chosen as $t_0 = 10^{-3}$. Since the thermal diffusion timescale is 4×10^5 [s], the initial heating time is about 400 [s]. At the onset of layer formation the temperature at the heated left wall has already reached its final value in all three cases. As is seen in Table 1, the 'reference' simulation corresponds to values of $Ra_\eta = 5 \times 10^4$ and

$R = 5$. The flow patterns at four different times are plotted in the Figs. 1(a–d) as contour plots of the streamfunction ψ. As time proceeds, convection cells form near the heated left boundary and gradually fill up the cavity with a layered flow. Cell formation happens almost simultaneously along the heated sidewall as would be expected for $Ra_\eta > Ra_{\eta,cr}$ [4]. Thus, final layers are formed in about 10 h and no subsequent layer merging is observed.

A vertical cross-section of the horizontal velocity at $x = 0.5$ and $t = 0.1$ (Fig. 2(a)) shows that the velocities differ in magnitude from layer to layer; typical maximal horizontal velocities are in the order of 10^{-5}–10^{-4} [m s^{-1}]. It was shown by ref. [8] that the flow within a layer (relatively far from the sidewalls) can be quite well approximated by a parallel flow driven by a layer averaged lateral temperature gradient $K(t)$. In dimensionless quantities, the equation for $u(z, t)$ follows from the dominant balance in (2b) between friction and buoyancy forcing, assuming a slow temporal variation of the lateral temperature gradient and the absence of a lateral salt gradient. In dimensionless form, the solution for the parallel flow becomes

$$u(z, t) = Ra_\eta K(t) \tfrac{1}{12}(2z^3 - 3z^2 + z) \tag{6}$$

where z is scaled with the layer thickness. In deriving (6), it is furthermore assumed that the horizontal velocity vanishes at the interfaces bounding the layer. It turns out that the vertical structure (6) is quite a good approximation of the horizontal velocity profiles for most of the layers in Fig. 2(a). For example, the flow profile in the well developed second convective layer is well fitted ($r^2 = 0.98$) through $u(z, t) = 1.4 \cdot 10^4 K(t) \frac{1}{12}(2.01z^3 - 3.01z^2 - 0.99z)$ which results, in comparison with (6), in almost the same position of the zeroes. The somewhat lower value of the estimated Rayleigh number indicates a flow which is not yet fully developed. A vertical cross-section of temperature and salinity at $x = 0.5$ (Fig. 2(b)) clearly shows the layered structure of the flow consisting of convection cells in which salt is fairly well mixed and temperature is stably stratified, separated by thin interfaces where the salt stratification is stable but the temperature stratification is unstable. Salt can be effectively used as a tracer due to its low molecular diffusivity. A shadow plot of the salinity in Fig. 2(c) shows that indeed the salt field is nearly homogeneous within the layers,

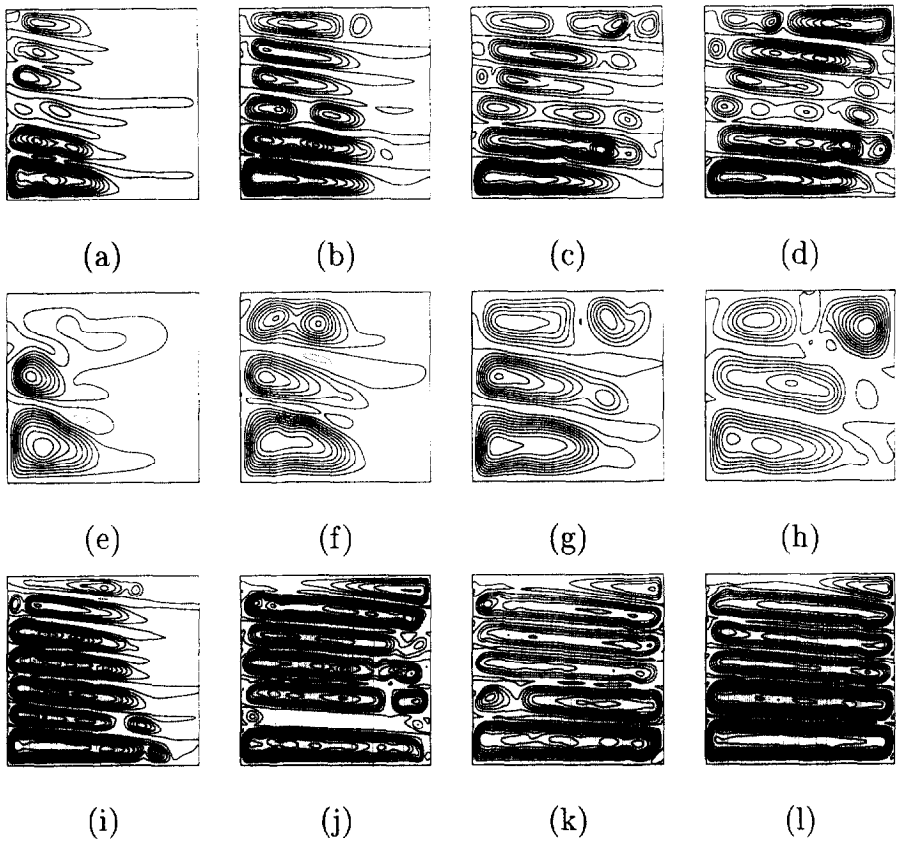

Fig. 1. Layer formation as a function of time shown by plots of the stream function: $Ra_\eta = 5 \cdot 10^4$, $R = 5$ (a–d); $Ra_\eta = 5 \cdot 10^4$, $R = 2.5$ (e–h); and $Ra_\eta = 2 \cdot 10^5$, $R = 5$ (i–l); (a, e, i): $t = 0.025$; (b, f, j): $t = 0.050$; (c, g, k): $t = 0.075$; (d, h, l): $t = 0.1$.

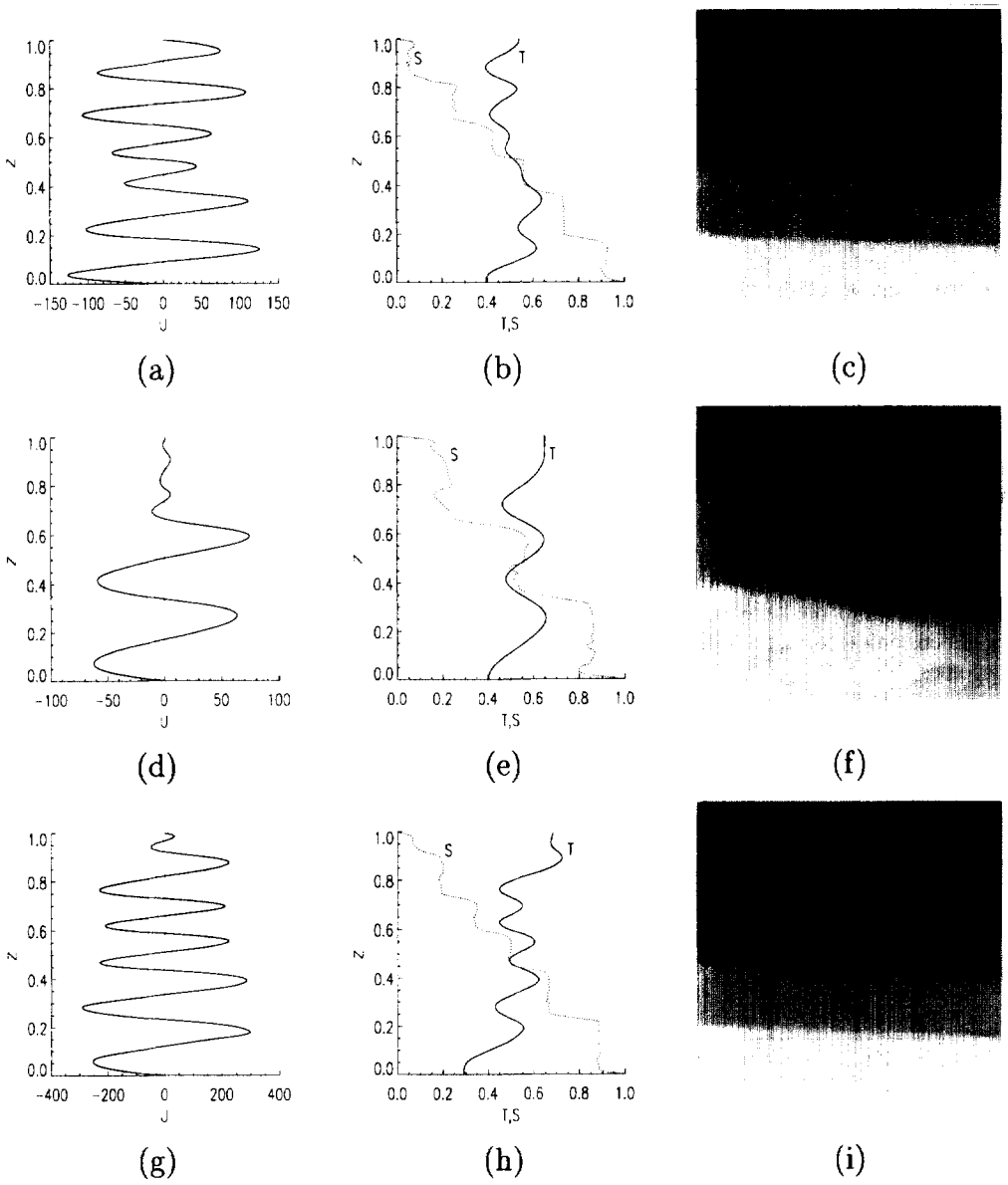

Fig. 2. Horizontal velocity (U), temperature (T) and salinity (S) profiles along a vertical section through the middle of the container and a grey-shade plot of the salinity field (white: salty, dark: fresh) at $t = 0.1$. (a–c) $Ra_\eta = 5 \cdot 10^4$, $R = 5$; (d–f) $Ra_\eta = 5 \cdot 10^4$, $R = 2.5$; (g–i) $Ra_\eta = 2 \cdot 10^5$, $R = 5$.

except near the right boundary, where the flow is not yet fully developed.

In the second simulation, the buoyancy ratio is lowered to $R = 2.5$ while keeping $Ra_\eta = 5 \times 10^4$ the same. From (4) it follows that the buoyant forcing measured by Ra_T is reduced considerably. The evolution of the flow (Fig. 1(e–h)) shows that the layers have increased in scale as is expected from a smaller R and also no subsequent layer merging occurs. At $t = 0.1$ the value of the horizontal velocities is smaller (Fig. 2(d)) than in the previous case, although one expects from (6) that the magnitude should be about the same, since it is proportional to Ra_η. The reason is that it takes longer for the flow to develop and at $t = 0.1$, the flow has not reached its maximum yet. This is also shown in the steps in the salinity profile (Fig. 2(e)) which are less pronounced than in Fig. 2(b) indicating that the salt is not well-mixed horizontally; this is confirmed in Fig. 2(f).

In the third simulation, Ra_η is increased to $Ra_\eta = 2 \times 10^5$ while $R = 5$ is the same as in the first simu-

lation. This implies a fourfold increase in buoyant forcing and the flow is seen to evolve much quicker (Figs. 1(i–l)) than in the two simulations discussed above. The larger buoyancy forcing induces the much larger horizontal velocities in Fig. 2(g), and these are more of equal magnitude in the different layers. The increase in velocity is only slightly smaller than the factor four increase expected from the idealized profile (6). The step structures are well-pronounced in the salinity and temperature profiles (Fig. 2(h)) and the salt is well-mixed within the layers (Fig. 2(i)). In all cases above, the number of final layers formed is $\mathcal{O}(R)$, which implies that the layers have a thickness of order η. The layer scale is therefore strongly dependent on R, whereas the time scale of evolution depends strongly on Ra_η.

An important observation from the large Ra_η case (Figs. 1(i–l)) is that there is a clear example of subsequent layer merging. The intrusions reach the cold wall before $t = 0.025$ (Fig. 1(j)) and about seven layers seem to form. However, during the evolution one of the layers disappears (Fig. 1(k)), leading eventually to a pattern of six cells at $t = 0.1$ (Fig. 1(l)). This merging process is similar to that observed, for example, in Fig. 18 of ref. [15], to which they refer to as class I merging. In subsequent sections, we will focus on this particular layer merging process by looking at several signatures of this process.

3.2. Heat and salt transport

The appropriate parameters that indicate the increase of transport due to convection are the vertically integrated horizontal heat transport and the horizontally integrated vertical salt transport. The nondimensional time in the simulation is just the Fourier number $Fo = t^* H^2/\kappa_T$ which is smaller than 0.1. Hence, the diffusive lateral heat transport $\mathcal{H}_d$ due to a temperature step (since the heating is relatively fast) is easily calculated from a one-dimensional semi-infinite layer approximation.

The local Nusselt number Nu associated with the horizontal heat transport and its vertical averaged value $\overline{Nu}$ are

$$Nu(x,z,t) = \frac{uT - \dfrac{\partial T}{\partial x}}{\mathcal{H}_d}; \quad \overline{Nu}(x,t) = \int_0^1 Nu(x,z,t)\,\mathrm{d}z. \tag{7a}$$

Similarly, the Sherwood numbers associated with the vertical salt transport are

$$Sh(x,z,t) = Le\,wS - \frac{\partial S}{\partial z}; \quad \overline{Sh}(x,t) = \int_0^1 Sh(x,z,t)\,\mathrm{d}x. \tag{7b}$$

The temporal development of $\overline{Nu}(0,t)$ and $\overline{Sh}(0,t)$ is shown in Fig. 3 for the three simulations in the previous section; for this case $\mathcal{H}_d(0,t) = (1/\pi t)^{1/2}$; for $t \to 0$ equation (7a) gives $Nu \to 1$ when there is only heat diffusion. As the layers have (almost) reached the right wall, Nu and Sh have the same order of magnitude in all three simulations. As the number of layers decreases for smaller buoyancy ratio, convective transport of salt becomes stronger and hence Sh increases (compare Figs. 3(a) and (b)). The lateral heat transport is nearly independent of R; the increase in heat transport due to larger layer thickness is compensated by a decrease due to smaller buoyancy forcing. Larger Ra_η gives larger velocities and consequently a larger heat and salt transport as shown in Fig. 3(c). In the latter case, one observes that $\overline{Nu}(0,t)$ approaches a value of about three near $t = 0.06$ but then increases again to have about a magnitude seven at $t = 0.1$. The increase in heat transport is a signature of the subsequent layer merging process, as observed in Figs. 1(g–i). A similar signature can be seen in the salt transport although it fluctuates much more than the heat transport.

3.3. Energy balances

The volume averaged kinetic and potential energy balances can be derived easily from the governing equations. A nondimensional density, the (local) kinetic energy E_k and potential energy E_p are defined as follows:

$$\rho = Ra_T(R\cdot S - T); \quad E_k = \tfrac{1}{2}(\mathbf{u}\cdot\mathbf{u}); \quad E_p = \rho z \tag{8a}$$

where $\mathbf{u} = (u, w)$ is the velocity vector. The global kinetic energy balance is derived by taking the inner product of $\mathbf{u}$ with the momentum balance and integrate the result over the flow domain Ω. One obtains

$$Pr^{-1}\frac{\mathrm{d}}{\mathrm{d}t}\langle E_k\rangle = \langle \mathbf{u}\cdot\nabla^2\mathbf{u}\rangle - \langle \rho w\rangle; \quad \langle\cdot\rangle = \int_\Omega \cdot\,\mathrm{d}x\,\mathrm{d}z. \tag{8b}$$

The global potential energy balance is obtained by multiplying (2c) with $-zRa_T$, (2d) with zRa_TR, add and integrate the result over the flow domain. This gives

$$\frac{\mathrm{d}}{\mathrm{d}t}\langle E_p\rangle = \langle \rho w\rangle - Ra_T(\langle z\nabla^2 T\rangle - R\,Le^{-1}\langle z\nabla^2 S\rangle). \tag{8c}$$

The evolution of terms in the kinetic and potential energy balances is presented in the Figs. 4 for the case $Ra_\eta = 2\times10^5$, $R = 5$. At all times, the primary kinetic energy balance is between viscous dissipation $\langle \mathbf{u}\cdot\nabla^2\mathbf{u}\rangle$ and buoyancy production by the flow (equal to $\langle -\rho w\rangle$) (Fig. 4(a)). The change in kinetic energy $\mathrm{d}\langle E_k\rangle/\mathrm{d}t$ is orders of magnitude smaller. Initially, from $t = 0$ to about $t = 0.025$, all terms in the kinetic energy balance increase in amplitude showing the evolution of the double-diffusive instabilities. Between $t = 0.025$ and about $t = 0.06$, both buoyancy production and dissipation remain fairly constant. Layer merging is associ-

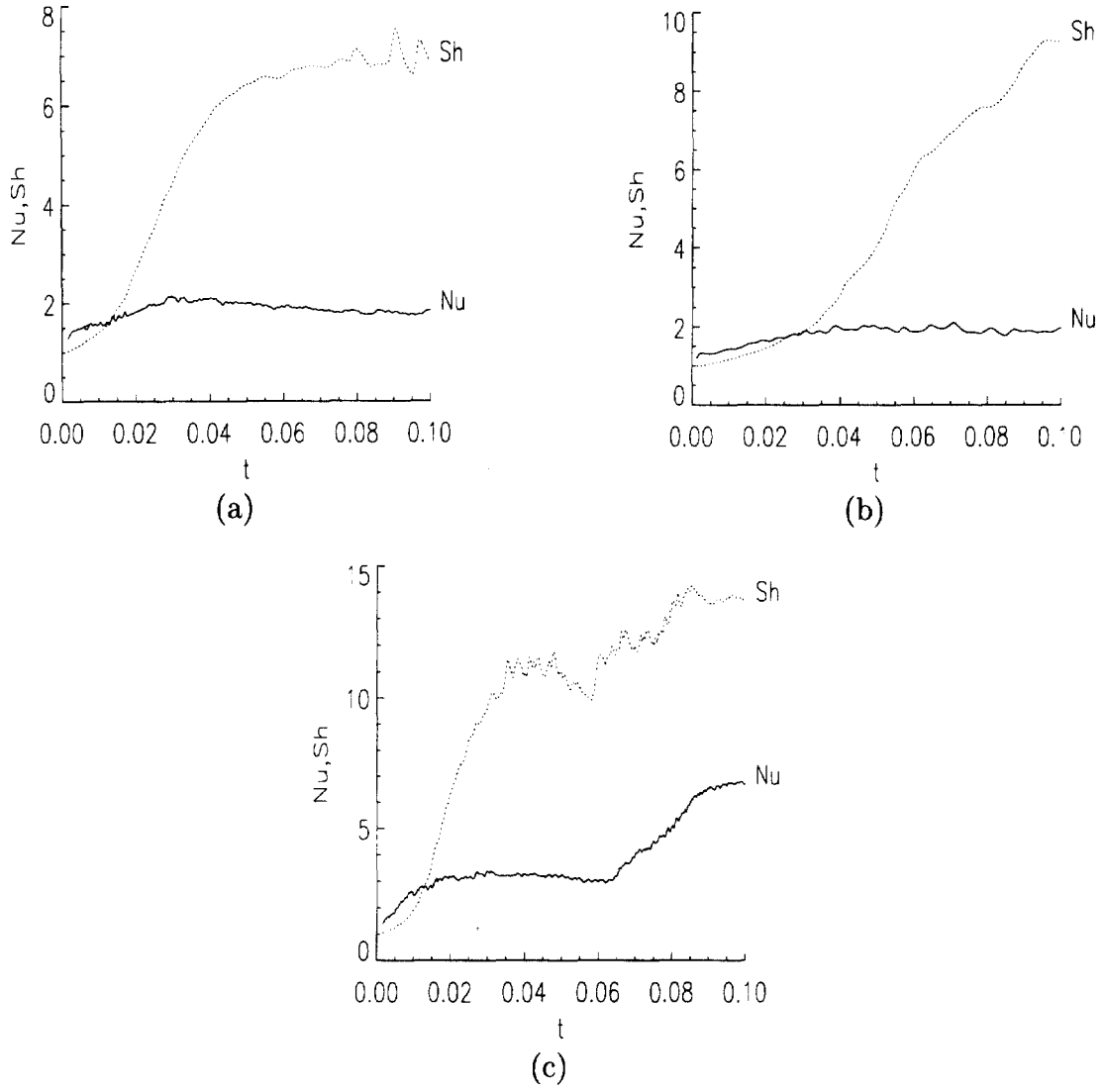

Fig. 3. Development in time of $\overline{Nu}$ (solid line) and $\overline{Sh}$ (dotted line): (a) $Ra_\eta = 5 \cdot 10^4$, $R = 5$; (b) $Ra_\eta = 5 \cdot 10^4$, $R = 2.5$; (c) $Ra_\eta = 2 \cdot 10^5$; $R = 5$.

ated with an increase in buoyancy production (and an increase of dissipation), since this term increases from $t = 0.06$ up to $t = 0.1$.

Because the Lewis number is large ($Le = 100$), the contribution of changes in the salt concentration and the salt fluxes at the boundaries of the flow domain to the change in potential energy (Fig. 4(b)) is small. The buoyancy production and the term $\langle z\nabla^2 T\rangle$ determine the change in potential energy. During the first stage of the evolution, this change is strongly negative since potential energy is converted into kinetic energy by the instability of the initial flow. During the merging process, the release of potential energy decreases and there is even a small interval, where the potential energy production is positive. The latter feature is absent at lower forcing (in the other two simulations considered) and is another signature of the layer merging process.

3.4. Analysis of flow details

We further investigate the layer merging as observed in the Figs. 1(i–l). In the Figs. 5, six shadow plots of the density are shown at different times between $t = 0.025$ and $t = 0.075$. In Fig. 5(a), the cross is at the same position as the one in Fig. 5(f). For ease of description, we label the disappearing layer with M and those bounding this layer above and below with M^+ and M^-, respectively. The interfaces bounding M clearly move to each

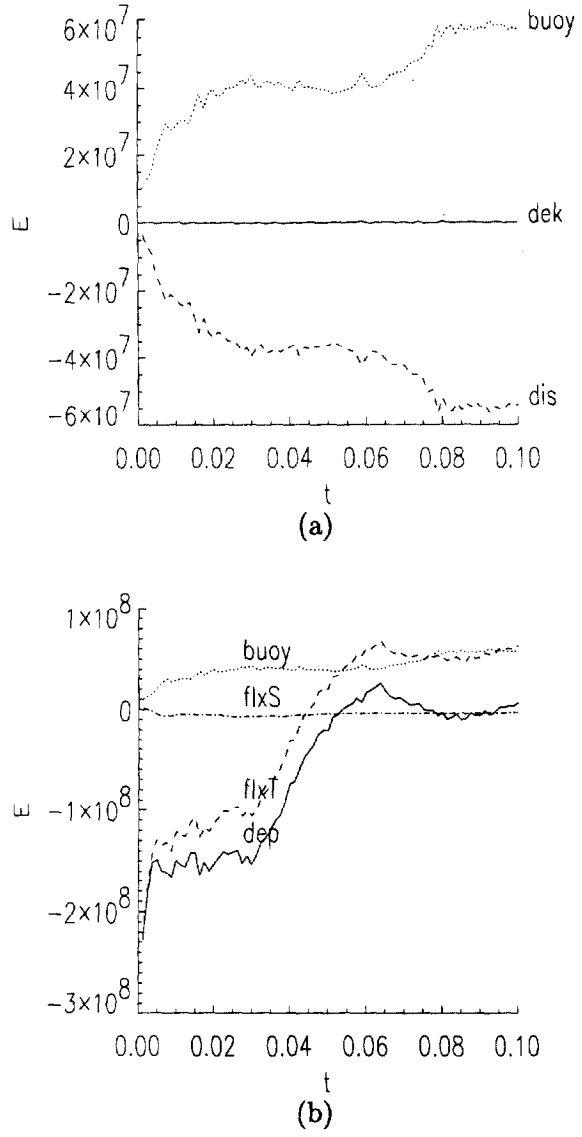

Fig. 4. The evolution of other terms in the kinetic and potential energy balances (8) for $Ra_\eta = 2 \cdot 10^5$, $R = 5$: (a) Kinetic energy balance; (b) Potential energy balance. Annotation: dek $= Pr^{-1}\mathrm{d}\langle E_k\rangle/\mathrm{d}t$ (change in kinetic energy), buoy $= -\langle \rho w\rangle$ (buoyancy production), dis $= \langle \mathbf{u}\cdot\nabla^2\mathbf{u}\rangle$ (viscous dissipation), dep $= \mathrm{d}\langle E_p\rangle/\mathrm{d}t$ (change in potential energy), flxT $= Ra_T\langle z\nabla^2 T\rangle$, flxS $= Ra_T R Le^{-1}\langle z\nabla^2 S\rangle$.

other during the merging and finally a new interface is established between M^- and M^+ nearly at the position halfway layer M before merging (Fig. 5(f)). This seems different from the usual interface migration [16] where one of the interfaces remains stationary. From the Figs. 5, it is not clear whether merging starts near the heated wall or elsewhere. At $t = 0.025$ (Fig. 5(a)), the interface between M and M^+ is vaguer near the heated wall, but at other times (for example Fig. 5(d)) the interface between M^- and M appears vaguer near the cold wall.

We first consider the evolution of the buoyancy jump between both interfaces bounding M. In Fig. 6, vertical sections are shown of the density at two positions ($x = 0.25$ and $x = 0.5$) within the layers. Although there are some locations where the flow appears unstably stratified, the results clearly show that merging is not related to the development of an unstable stratification and subsequent mixing. This supports the hypothesis made by ref. [7] that an unstable stratification is not necessary for layer merging to occur. By comparing the profiles at both locations, it is observed that the layer M disappears first at $x = 0.25$ and later on at $x = 0.5$ (Fig. 6(d)), supporting the view that layer merging starts at the heated wall. In Fig. 7, the horizontal velocity and the temperature are plotted along the same sections. The horizontal velocity within the layer M decreases to zero and the unstable temperature stratification over both the interfaces bounding layer M is eroded during the merging process. There appears to be a phase lag in this development between the evolution of the temperature and the horizontal velocity profile, with the former leading the latter. The interface M is shown to disappear earlier in the temperature profile than in the horizontal velocity profile. By only looking at the temperature, the layer M appears to disappear first at $x = 0.5$ rather than at $x = 0.25$ (Fig. 7(b)–(c)) contrary to that seen for the density in Fig. 6. The salt field clearly is important for the changes in the spatial pattern during the layer merging process.

The results in Fig. 7 motivate to look at the origin of the velocity decrease within layer M. According to (6), the horizontal velocity can change due to variations in the layer thickness (h) or changes in the lateral temperature gradient ($K(t)$). By computing the horizontal heat balance over a vertical section of the layer [8], it can be shown that the lateral temperature gradient depends on changes in layer thickness. However, when the spatial gradients in the layer thickness remain small, as is observed in Fig. 5, this effect is small and $K(t)$ can be assumed constant during the layer merging.

Changes in layer thickness may be caused by changes in the entrainment rate [1]. This motivates to look for a measure of this entrainment rate, i.e. the Richardson number, defined by

$$Ri = -\frac{\dfrac{\partial \rho}{\partial z}}{\left[\dfrac{\partial u}{\partial z}\right]^2}. \tag{9}$$

At $t = 0.0375$, which is before merging, shadow plots of the salinity and Ri are shown in Fig. 8(a) and Fig. 8(b), respectively. In Fig. 8(b), a dark area indicates locations where Ri is relatively small, whereas it is relatively large at light areas; more precise shading values are given in

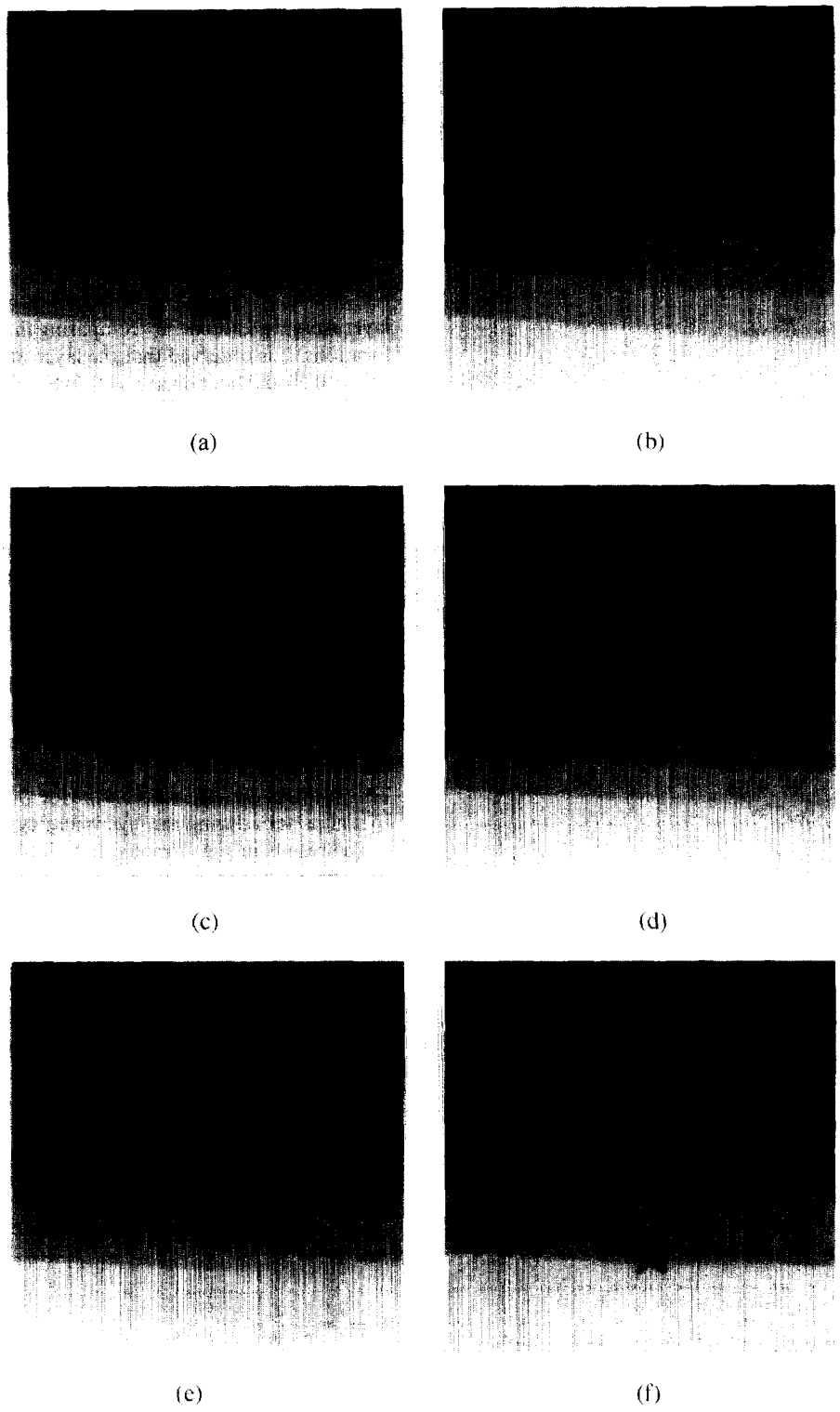

Fig. 5. Density profiles showing subsequent layer merging, $Ra_\eta = 2 \cdot 10^5$, $R = 5$, the cross in (a) and (f) are on the same position: (a) $t = 0.025$; (b) $t = 0.03125$; (c) $t = 0.0375$; (d) $t = 0.05$; (e) $t = 0.0625$; (f) $t = 0.075$.

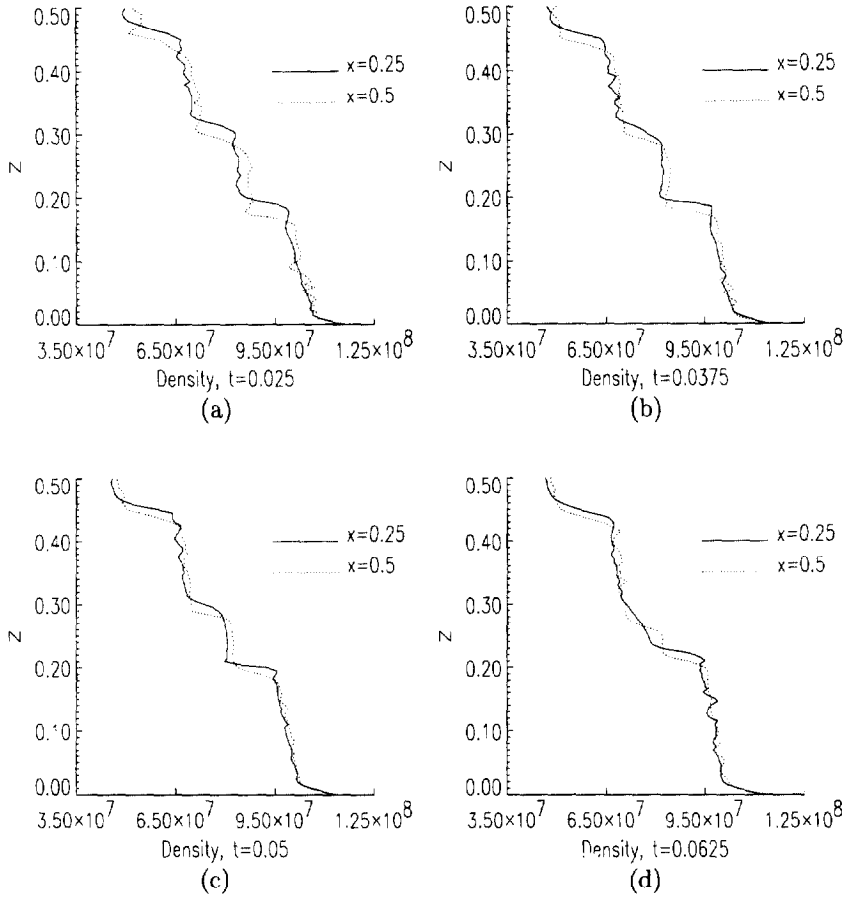

Fig. 6. The subsequent merging process revealed by two vertical sections (near the wall and through the centre) of the density at different instants. For clarity only the lower half of the sections is shown: (a) $t = 0.025$; (b) $t = 0.0375$; (c) $t = 0.05$; (d) $t = 0.0625$.

the caption. Within the layers, Ri is smaller than zero, which is characteristic of strong convective activity. However, along an interface Ri increases from the heated wall to the cold wall. A smaller value of Ri indicates a less stable interface between layers, and a larger entrainment rate is expected.

The position of the interface is determined by the location where the horizontal velocity changes sign. In Fig. 8(c), the values of Ri exactly at the interfaces between M and M^+ and between M and M^- (at $x = 0.1$) are plotted at several instants prior to merging. During merging, where layer M ceases to exist, the values of Ri of the surrounding interfaces strongly increase, indicating that these interfaces become more stable.

4. Discussion

The results from the two-dimensional numerical simulations of the evolution of intrusions into a stratified liquid show many features also observed in experiments. This a postiori justifies the use of the two-dimensional model; the dominant physics of layer formation and merging is captured by such a model. Focus of this work was on the subsequent layer merging process as observed in one of the simulations. Based on these results we propose the following physical picture of this process.

Again, we refer to the layers M, M^- and M^+ as the layer which eventually disappears, its lower and its upper neighbour, respectively. The results on the distribution of Ri indicate (Fig. 8(b)) that the entrainment rate along the interface bounding M and M^- is not constant along the interface. Assume now that the interface between M and M^- is locally displaced upward. Since the velocity gradients in layer M^- are largest near the heated wall (giving smaller Ri), largest displacements will occur there. By the direct change in the layer thickness, the horizontal velocity, according to (6), locally decreases in layer M whereas it increases in layer M^-. The higher velocities in layer M^- then lead to a larger entrainment upwards

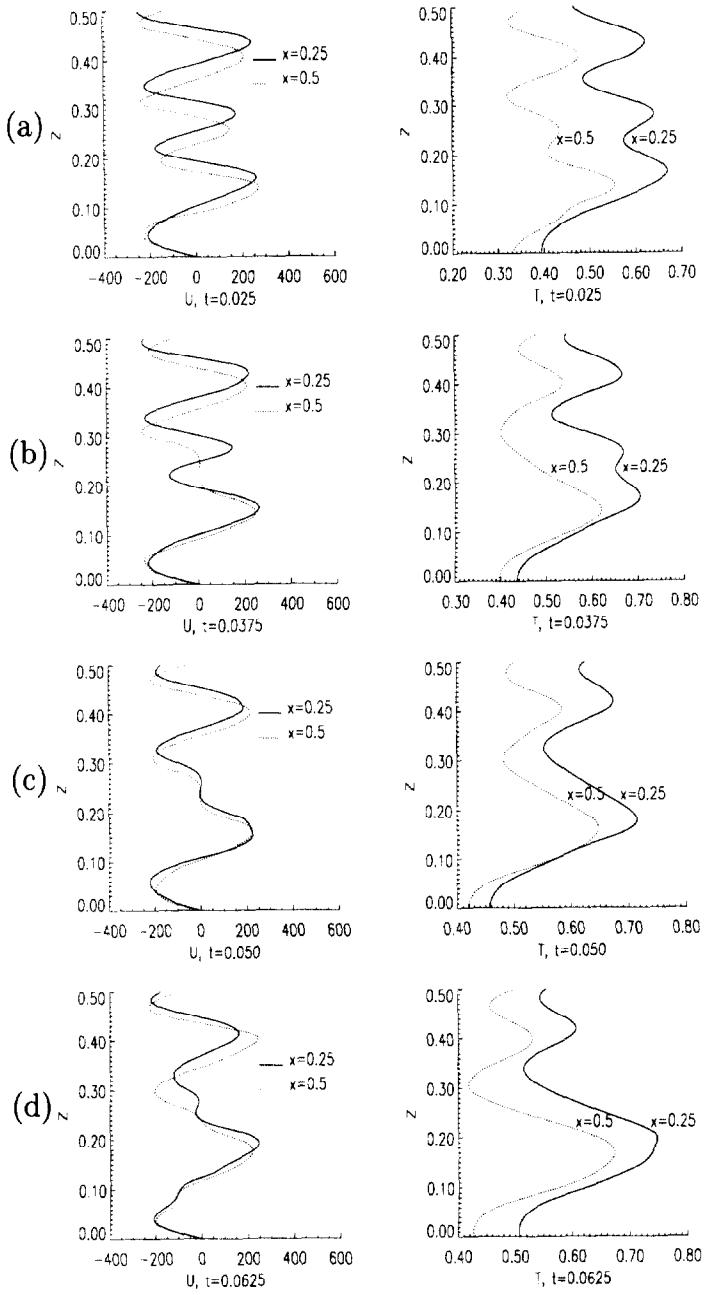

Fig. 7. Cross-sections of the horizontal velocity U and temperature T, as in Fig. 6; again only the lower half of the sections is shown: (a) $t = 0.025$; (b) $t = 0.0375$; (c) $t = 0.05$; (d) $t = 0.0625$.

and thereby to a further displacement of the interface upwards. This view is also consistent with the observation of ref. [7] that the thermal boundary layer near the heated wall penetrates the interface and locally destroys the salinity step. Because the velocities in layer M decrease, the stronger convection in layer M^+ will cause a downward migration of the interface between M and M^+.

Hence, the interfaces bounding M and M^- and M and M^+ move towards each other, consistent with observations in the Figs. 6 and 7. Because the velocities increase in both layers M^- and M^+, the buoyancy production increases (Fig. 4) and the horizontal heat transport as well as the vertical salt transport increases (Fig. 3). As the interfaces have reached each other and layer M has disappeared, the stability of the resulting interface increases because of the larger density difference over the

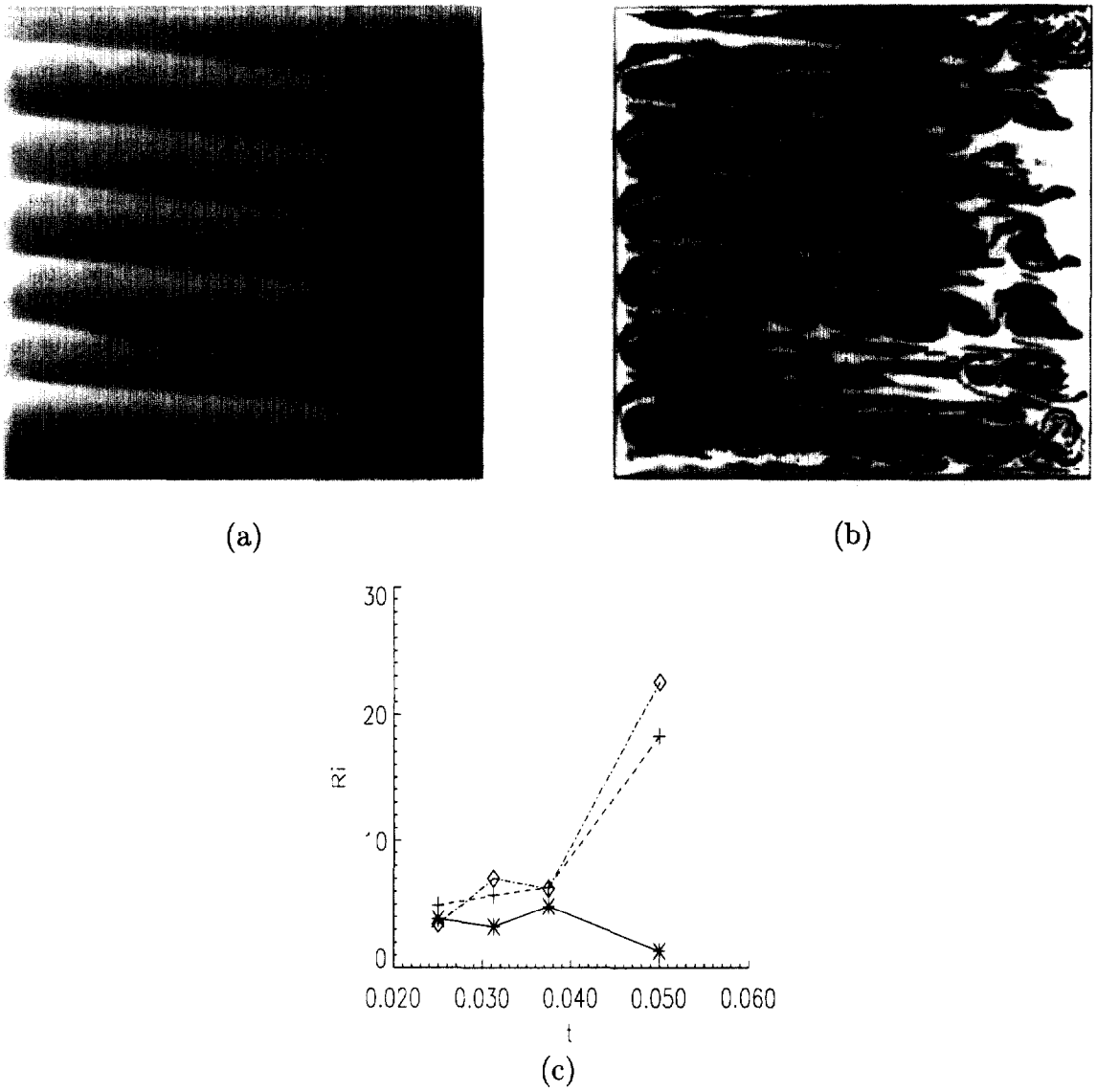

Fig. 8. (a) Grey-shade plot of salinity minus initial stratification at $t = 0.0375$, just before subsequent merging sets in; white corresponds to a maximum and black to a minimum in salinity. (b) The same as (a) but for Ri; white corresponds to $Ri \geqslant 16$, black corresponds to $Ri \leqslant 0$. (c) Temporal development of Ri near the heated wall ($x = 0.1$) for the first three interfaces from below. The results for the first, second and third interface are annotated with a plus, star and diamond, respectively. At $t = 0.06$ and beyond, the second interface does not exist anymore.

newly formed interface (Fig. 6). This is reflected in the larger values of Ri of this interface after merging (Fig. 8(c)) and also in the positive potential energy production found in Fig. 4(b), which indicates a restratification of the flow.

An alternative, dynamical systems point of view of this process is obtained using the results presented in ref. [14]. In the unicellular flow regime, many (unstable) steady states exist at large Ra_{η}. It was shown that a trajectory may remain a very long time near such an unstable state. Eventually, this state is left through an instability and the flow evolves to a situation with more layers. Although the instability mechanism was difficult to describe, it was suggested to be associated with the movement of the interface between the layers. In view of the description of the physics above, this instability may be identified in terms of the feedback between differential entrainment and changes in the layer thickness.

One can view the flow prior to merging to be near such an unstable steady state, to which the flow trajectory

is attracted along the stable manifold. The differential entrainment along the interfaces separating the layers can be considered as finite amplitude perturbations on this unstable steady state. Because many steady states are present, these perturbation easily induce a transition to another state with less layers. The transitions are basically dependent on how differential entrainment is able to drive the trajectory into the unstable manifold of the underlying steady state prior to merging. This view may explain why different experiments, with the same set-up and parameters, are likely to give very different merging sequences.

Acknowledgements

All computations were performed on the CRAY C90 at the Academic Computing Centre (SARA), Amsterdam, the Netherlands within the project SC212. Use of these computing facilities was sponsored by the Stichting Nationale Supercomputer faciliteiten (National Computing Facilities Foundation, NCF) with financial support from the Nederlandse Organisatie voor Wetenschappelijk Onderzoek (Netherlands Organization for Scientific Research, NWO). The authors thank Jeroen Molemaker for the use of the explicit CFD code and for comments on the results.

References

[1] Turner JS. Buoyancy effects in fluids. Cambridge, 1973.
[2] Akbarzadeh A, Manins P. Convective layers generated by side walls in solar ponds. Solar Energy 1988;41(6):521–9.
[3] Thangam S, Zebib A, Chen CF. Transition from shear to sideways diffusive instability in a vertical slot. J Fluid Mech 1981;112:151–60.
[4] Chen CF, Briggs DG, Wirtz. Stability of thermal convection in a salinity gradient due to lateral heating. Int J Heat Mass Transfer 1971;14:57–65.
[5] Huppert HE, Turner JS. Ice blocks melting into a salinity gradient. J Fluid Mech 1980;100:367–84.
[6] Lee JW, Hyun MT, Kang YS. Confined natural convection due to lateral heating in a stably stratified solution. Int J Heat Mass Transfer 1990;33:869–75.
[7] Tanny J, Tsinober AB. The dynamics and structure of double-diffusive layers in sidewall-heating experiments. J Fluid Mech 1988;196:135–56.
[8] Jeevaraj C, Imberger J. Experimental study of double-diffusive instability in sidewall heating. J Fluid Mech 1991;222:565–86.
[9] Kerr OS. Heating a salinity gradient from a vertical sidewall: nonlinear theory. J Fluid Mech 1990;217:529–46.
[10] Kamagura K, Ozoe H. Experimental and numerical analyses of double diffusive convection. Int J Heat Mass Transfer 1993;36:2125–34.
[11] Lee JW, Hyun JM. Double diffusive convection in a cavity under a vertical solutal gradient and a horizontal temperature gradient. Int J Heat Mass Transfer 1991;34:2423–7.
[12] Tsitverblit N, Kit E. The multiplicity of steady flows in confined double-diffusive convection with lateral heating. Physics Fluids A 1993;5:1062–4.
[13] Kranenborg EJ, Dijkstra HA. The structure of (linearly) stably double diffusive flow patterns in a laterally heated stratified liquid. Physics of Fluids 1995;7:680–2.
[14] Dijkstra HA, Kranenborg EJ. A bifurcation study of double-diffusive flows in a laterally heated stably stratified liquid layer. Int J Heat Mass Transfer, in press, 1997.
[15] Schladow SG, Thomas E, Koseff JR. The dynamics of intrusions into a thermohaline stratification. J Fluid Mech 1992;236:127–65.
[16] Linden PF. The formation and destruction of fine-structure by double-diffusive processes. Deep-Sea Res 1976;23:895–908.